Coupled-cavity AlInAs/InGaAs/InP quantum cascade lasers fabricated by focused ion beam processing

JPhys Photonics

PAPER

Coupled-cavity AlInAs/InGaAs/InP quantum cascade lasers fabricated by focused ion beam processing

Kamil Pierściński[1], **Maciej Bugajski**[1], **Tomasz Czyszanowski**[2], **Andrzej Kolek**[3], **Marek Wesołowski**[4], **Maciej Kuc**[2], **Robert P Sarzała**[2], **Maciej Dems**[2], **Mariusz Płuska**[1], **Dorota Pierścińska**[1], **Włodek Strupiński**[4] and **Andrzej Czerwiński**[1]

[1] Institute of Electron Technology, Al. Lotników 32/46, 02-668 Warszawa, Poland
[2] Lodz University of Technology, Institute of Physics, Photonics Group, Wólczańska 219, 90-924 Łódź, Poland
[3] Department of Electronics Fundamentals, Rzeszów University of Technology, 35-959 Rzeszów, Poland
[4] ENT SA, Al. Szucha 8, 00-582 Warszawa, Poland

E-mail: bugajski@ite.waw.pl

Keywords: quantum cascade laser (QCL), coupled-cavity (CC) laser, focused ion beam processing

OPEN ACCESS

RECEIVED
19 June 2018

REVISED
15 September 2018

ACCEPTED FOR PUBLICATION
30 October 2018

PUBLISHED
6 December 2018

Abstract

Focused ion beam processing has been applied to fabricate coupled-cavity AlInAs/InGaAs/InP quantum cascade lasers. The evolution of the mode spectrum of the two coupled Fabry–Perot cavities, controlled by the driving currents of both sections leading to single mode operation, has been observed. Theoretical analysis of the observed behavior, supported by extensive numerical modeling is given. The analysis showed that the most efficient single mode operation takes place in the case of relatively close current densities in both sections of coupled-cavity quantum cascade lasers, which assures the overlap of the gain spectra. In such a configuration, fine tuning of the currents allows the favoring of the mode that coincides with gain peaks and suppresses all others.

1. Introduction

Quantum cascade lasers (QCLs) utilise the optical transitions between quantized states of electrons in a conduction band that allows versatile control of the emission wavelength by a heterostructure design [1]. The available QCL's emission wavelength spans a broad infrared range, where many gases have their absorption spectra [2]. QCLs are typically fabricated in Fabry–Perot geometry, which suffers from multi-longitudinal mode emission. For chemical sensing, however, there is a need for single-mode sources. Therefore, the concept of distributed feedback (DFB) was applied to achieve the desired emission characteristic. DFB QCLs proved their efficiency in that matter, allowing a single mode emission with a high side mode suppression ratio (SMSR) above 50 dB [3] in a broad range of steering currents. The complicated technology, which typically requires a multi-step growth, is the main disadvantage of DFB QCLs.

Here we use a coupled-cavity (CC) approach as an alternative to DFB QCLs. CC QCLs can be realized by cutting a slot across their cavity, dividing the laser into two unequal, electrically separated sections, which can be driven independently. Two CCs share the longitudinal modes favoring only those which meet the resonance condition in both cavities, and can be efficiently enhanced by the gain spectrum [4]. It has been demonstrated that focused ion beam etching (FIB) might be an ideal tool for the post-processing of quantum cascade lasers aimed at the fabrication of CC stable single mode lasers [5–9].

In comparison to DFB QCLs, FIB fabrication of CC QCLs is technologically less demanding and can be done on preselected structures, increasing the fabrication yield of devices with a specific wavelength. We show that a simple technique of cutting the cavity facilitates the single longitudinal mode operation of a high SMSR.

The paper is organized as follows. In section 2, we describe the single cavity QCL structure and detail its design. In section 3, the focused ion beam method is described, which is used to process the QCL lasers into CC structures. In section 4 we report the emission spectra of a CC QCL. In section 5 we describe the numerical

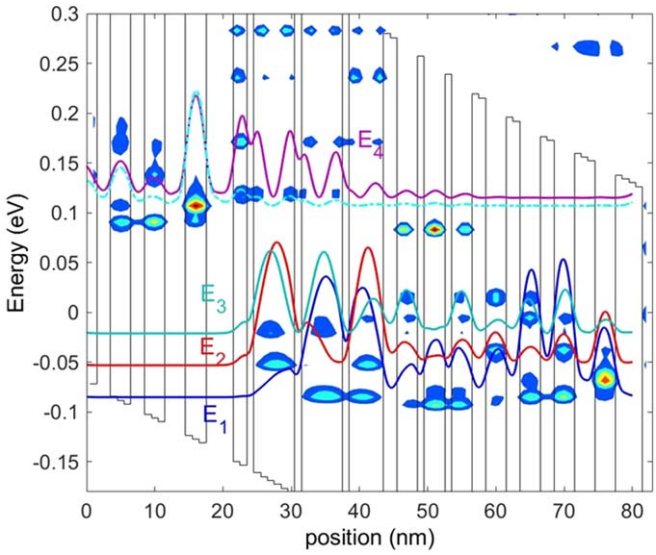

Figure 1. Conduction band profile and spectral functions at the energies of laser levels calculated for injector/active/injector segment of the laser under an applied field F = 29 kV cm^{-1} (close to threshold). The E_4, E_3, E_2 and E_1 refer to the upper, lower and ground state doublet of lasing transitions. The lowest energy state in the injector is also shown (light blue).

Table 1. Layer structure of AlInAs/InGaAs/InP laser.

1.0 μm	InP	n = 1e19 cm^{-3}	cladding
1.5 μm	InP	n = 1e17 cm^{-3}	waveguide
1.5 μm	InP	n = 3e16 cm^{-3}	
1.88 μm	30 x AlInAs/InGaAs		active region
1.5 μm	InP	n = 3e16 cm^{-3}	waveguide
1.5 μm	InP	n = 1e17 cm^{-3}	
500 μm	InP	n = 2e18 cm^{-3}	substrate

model used in the analysis of optical spectra. We compare simulations with experimental results, and demonstrate the ability of the single mode operation of the device. Finally, conclusions are brought in section 6.

2. Laser design

The lattice matched (~9 μm) $Al_{0.48}In_{0.52}As/In_{0.53}Ga_{0.47}As$/ InP QCLs are grown by metalo-organics vapor phase epitaxy on n-type InP in Aixtron AIX200/4 horizontal reactor. The active region of the lasers is of a 4-well 2-phonon resonance design [10–12]. The layer sequence of one period of the structure, in nanometers, starting from the injection barrier is: **4.0**, 1.9, **0.7**, 5.8, **0.9**, 5.7, **0.9**, 5.0, **2.2**, 3.4, **1.4**, 3.3, **1.3**, 3.2, **1.5**, 3.1, **1.9**, 3.0, **2.3**, 2.9, **2.5,** 2.9 nm. The AlInAs barriers are denoted in bold, the InGaAs wells are in normal font. The total thickness of one period is 62.8 nm. The laser structure consisted of the 30 periods.

The conduction band profile and spectral functions at the energies of the levels involved in light generation in the injector/active/injector segment of the QCL under the applied field of 29 kV cm^{-1} are shown in figure 1. Calculations were performed within non-equilibrium Green's function (NEGF) formalism [13]. This method enables the easy implementation of open boundaries, position and energy dependent effective mass and returns spectral function with the (position) shape corresponding to squared wavefunction for a given eigenenergy.

The structure uses a symmetrical, lightly doped InP waveguide for transverse mode confinement. The details of the layer structure of the laser are listed in table 1.

The double trench lasers were fabricated using standard processing technology, i.e., wet etching and Si_3N_4 for electrical insulation. The low resistivity Ti/Pt/Au ohmic contact to epi-side and AuGe/Ni/Au to the substrate were used. The contacts were RTA alloyed. For current injection, windows were opened through the insulator with a width of 10 μm or 15 μm. The lasers were cleaved into bars of 2 mm long and directly Au-Au bonded epi-side up to AlN submounts and then to copper mounts [11, 12].

Waveguide losses have been calculated using a 2D complex mode solver FIMWAVE Photon Design [14]. For the cavity length $L = 2$ mm, and the waveguide losses $\alpha_W = 6.07$ cm^{-1}, the total losses including mirror losses

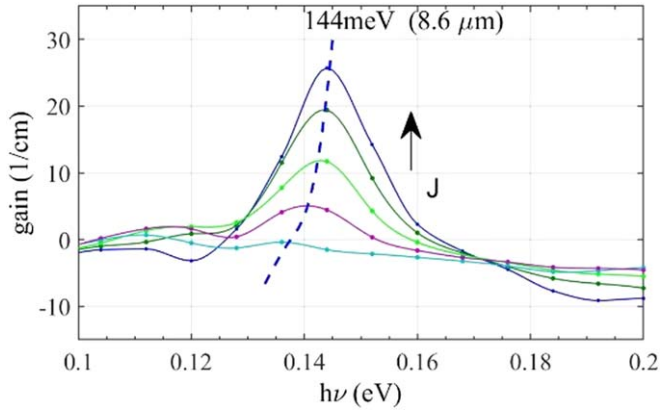

Figure 2. Spectral distribution of gain in an $Al_{0.48}In_{0.52}As/In_{0.53}Ga_{0.47}As/InP$ ($\lambda = 9$ μm) laser at room temperature for different values of driving the current ranging from 3.0 kA cm^{-2} to 5.5 kA cm^{-2}.

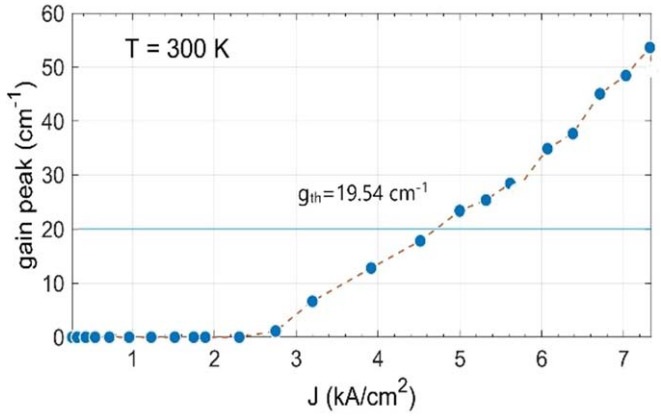

Figure 3. Peak gain as a function of current density calculated for an $Al_{0.48}In_{0.52}As/In_{0.53}Ga_{0.47}As/InP$ ($\lambda = 9$ μm) laser.

and losses in heavily doped contact layer $\alpha_W + \alpha_M + \alpha_{PW} = 15.55$ cm^{-1}, which for $\Gamma_{AR} = 0.796$ gives the threshold gain $g_{th} = 19.54$ cm^{-1}.

The NEGF method allows for the examination of electron transport, optical gain, and carrier distributions in the subbands of the laser [15, 16]. The problem is completely solved in the k-space and nonparabolicity accounted through energy dependent effective mass. Scattering self-energies included in NEGF formalism are for LO-phonon, interface roughness, alloy disorder ionized impurity and energy averaged LA-phonon scattering. Electron-electron scattering was included within the Hartree approximation by solving the Poisson equation (with the boundary conditions that preserve charge neutrality of each QCL period) self-consistently with NEGF equations. Calculated spectral distribution of the gain is shown in figure 2.

Maximum gain is observed at the wavelengths $\lambda \sim 8.6$–9.0 μm, being in good agreement with the lasing frequency. The dependence of peak gain on current density is shown in figure 3. As can be seen, the threshold gain should be reached at about 4.65 kA cm^{-2}.

3. Focused ion beam processing

To obtain CC-QCL, a slot within the mesa of a Fabry–Perot-QCL was milled with the use of an FIB. For this purpose, a dual-beam Helios Nano Lab 600 system (with both, electron beam and ion beam columns) was used. Ion milling processes were performed with focused Ga^+ ion beam at 30 kV accelerating voltage. Various ion beam currents were used at different stages of etching [17].

To enable FIB processing, QCLs were mounted epi-side up. The SEM images of an exemplary laser after processing are shown in figure 4. The laser of 2 mm length was cut in 1:3 proportions. The mesa which forms the lateral limits of the waveguide is visible in the middle of the structures.

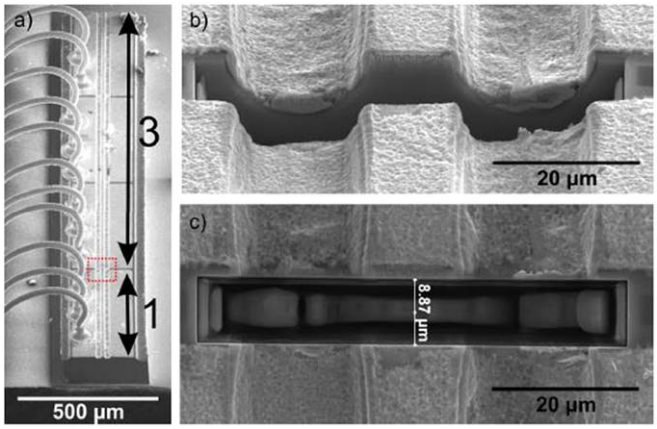

Figure 4. The SEM images of an exemplary laser after processing. (a) Top view of the laser, (b) side view of the slot being magnification of the region assigned by the red rectangle in (a). (c) Top view of the slot. The width of the gap was 8.87 μm.

Lasers with two types of metallization were used. One type of laser had a thick layer of galvanic metallization at the top of whole structure. This thick layer of metallization formed a strong obstacle in the manufacturing of CC QCLs with FIB. The other lasers had contact metallization only. To form a CC QCL, a rectangular gap within the mesa was ion milled. Additionally, metallization outside the mesa was removed to provide electrical separation of both sections.

Intuitively, it seems that a coarse, rectangular gap is to be etched, and then two opposite edges of the gap, which will act as the mirrors, need to be cleaned up. In such an approach, a serious problem occurs; when one mirror is cleaned, the milled material of the structure deposits on the other sides of the gap. This contamination by unwanted deposition should be avoided because it may degrade the optical performance of newly formed mirrors at both laser sections (the walls perpendicular to the optical path). Moreover, it can form short-circuit across the laser structure. Although trench sides parallel to the optical path do not form mirrors (and therefore they seem not to be necessarily cleaned up), the above requirements apply also to these trench walls due to possible short-circuiting.

To decrease the effect of secondary deposition instead of typical milling of the final shape of the gap with each side etched separately, all four sides of the gap need to be cleaned up during each pass of the ion beam. In this case, to obtain a clear slot sides with the designed length of this gap, the cleaning of the edges consists of etching several rectangular frames. Subsequently, at the next stages of the FIB milling (with a decreased ion beam current), these frames have been extended in all directions to obtain the desired length and width of the gap. The same procedure applies to cutting the metallization when separating electrically two QCL sections outside of the laser mesa region.

We have also used lasers processed with a special set of masks for which metallization consisted of 500 μm length segments separated by 20 μm gaps. In this case, slots were etched directly in semiconductor material, which greatly simplifies the ion milling procedure.

The quality of mirrors obtained with FIB was checked by the comparison of threshold currents fro m a test QCL before and after the FIB milling of one of its mirrors (i.e. cutting it by several micrometers). The threshold current of this QCL after the FIB milling changed by less than 10%, i.e. the FIB milling didn't deteriorate the quality of the mirror in comparison with the mirror quality before the FIB processing. The capability to observe the FIB processes *in situ* with the scanning secondary electron mode (using electron column) and scanning ion beam microscope mode (obtained by bombardment with scanning ion beam and detection of secondary electrons) gave unique control over the technological processes.

4. Experimental characterization

An experimental characterization included the measurement of pulsed light-current-voltage (LIV) curves and spectral measurements. LIV characteristics were registered using a high-voltage pulser and a fast, sensitive MCT detector for a measurement of the emitted power. The spectral characteristics were registered by means of a Fourier transform spectrometer (Nicolet 8700) equipped with an LN2 cooled MCT detector. Spectral resolution of the spectrometer is 0.125 cm^{-1}. To achieve optimal collection efficiency, the light emitted by the QCL was collimated using a reflective objective.

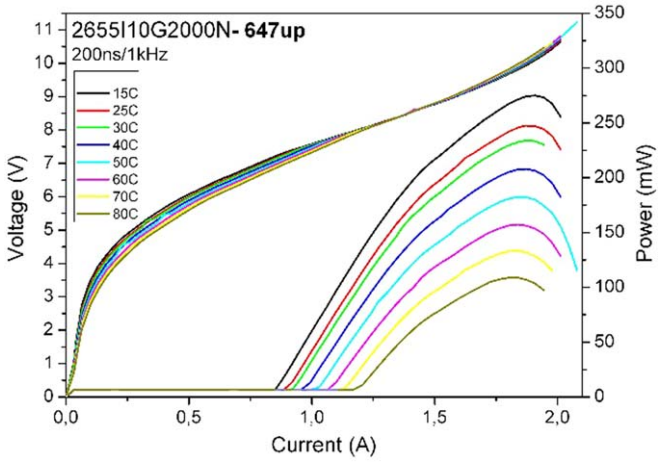

Figure 5. Room temperature light–current and current-voltage characteristics of the $Al_{0.48}In_{0.52}As/In_{0.53}Ga_{0.47}As/InP$ ($\lambda = 9$ μm) laser driven by 200 ns pulses with a repetition rate of 1 kHz. The laser cavity length equals 2 mm and the mesa width equals 10 μm.

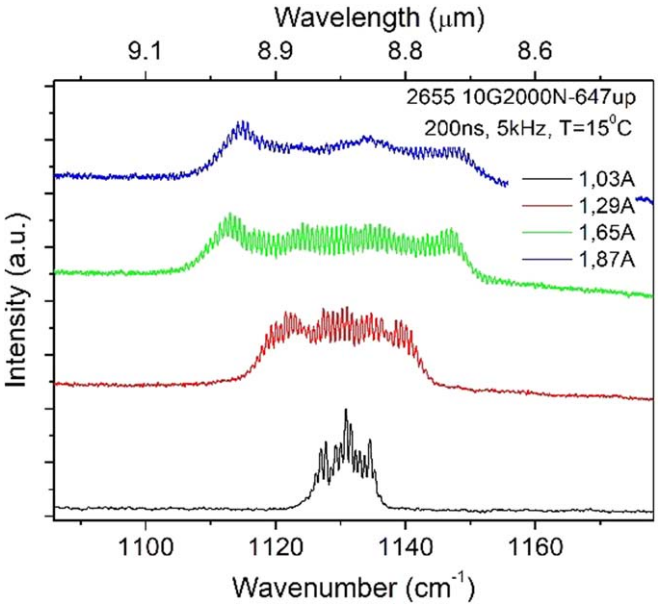

Figure 6. The emission spectra of an unprocessed QCL for different currents above threshold at room temperature.

Light–current and current-voltage characteristics of the unprocessed $Al_{0.48}In_{0.52}As/In_{0.53}Ga_{0.47}As/InP$ device are shown in figure 5. The threshold current density at room temperature equals $J_{th} = 4.55$ kA cm^{-2}, whereas the emitted optical power exceeds 250 mW per facet. At T = 80 °C, the laser still emitted ~100 mW per facet. The threshold voltage V_{th} was equal to ~7 V at room temperature.

Figure 6 presents the spectrum of an unprocessed QCL. A typical, multimode emission spectrum is registered, corresponding to a long Fabry–Perot type resonator.

After the initial characterization, the device was processed by the FIB milling to obtain CC QCL. In the case of a two-section device, each section was biased with an independent power supply. Current pulses delivered to each section were synchronized by means of an external pulse generator, additionally allowing the changing of the delay between two synchronized pulses.

The introduction of the gap results in the modification of spectral characteristics. Namely, the coupled resonator exhibits larger spectral spacing between the longitudinal modes and the number of modes is greatly reduced. To obtain single mode operation, it is necessary to tune the device by applying the appropriate current pulses to the long section (LS) and the short section (SS). Figure 7 presents the spectra of the CC QCL with both sections being operated.

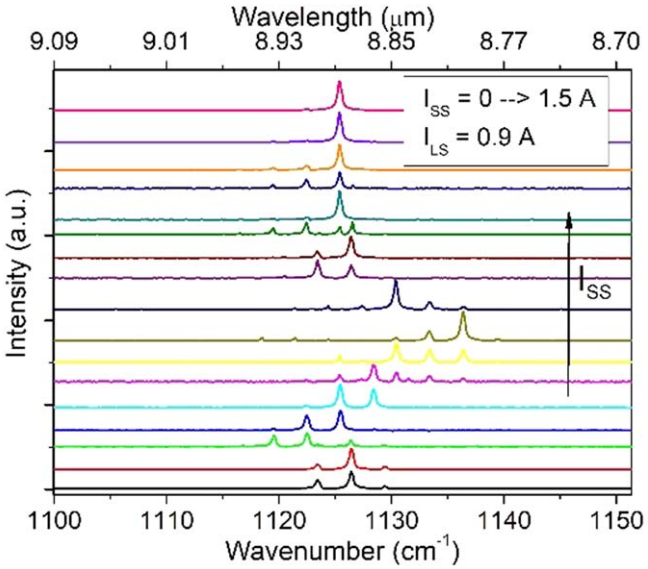

Figure 7. Evolution of room temperature mode spectrum of a CC QCL at LS current fixed above threshold, and the SS current varying from 0 to well above threshold.

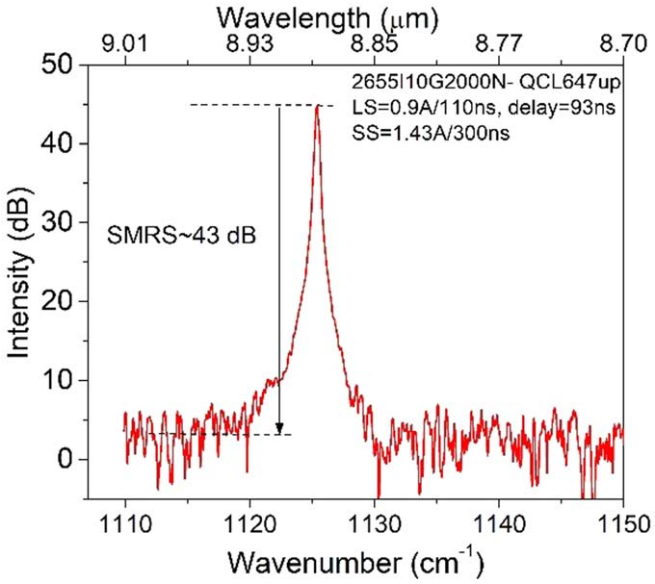

Figure 8. Single mode spectrum of CC QCL at room temperature exhibiting a side-mode suppression ratio equal to 43 dB.

The long section was biased above threshold and its current was kept constant at $I_{LS} = 0.9$ A ($I_{th(LS)} \sim 0.7$ A), whereas the short section current I_{SS} was changed from 0 to 1.5 A. The short section acts as a passive filter. As the I_{SS} current increases, the short section heats up, which results in the appropriate shift of CC modes. For I_{SS} currents, referring to the transmission resonance CC favours excitation of one dominant mode. A single mode operation of a CC QCL was obtained at ~1125 cm^{-1} with an SMSR of 43 dB. (see figure 8). The full-width of half maximum of the dominating mode was equal to 0.69 cm^{-1}. The laser exhibited output power of ~25 mW per facet at room temperature.

The short section was operated at $I_{SS} = 1.43$ A, a pulse length 300 ns, long section at $I_{LS} = 0.9$ A and pulse length 110 ns. Both sections were driven with a repetition rate 5 kHz, from separate pulse generators. The delay between SS and LS pulses was 93 ns, which refers to the intra-pulse time constant for achieving a steady state temperature by the short section.

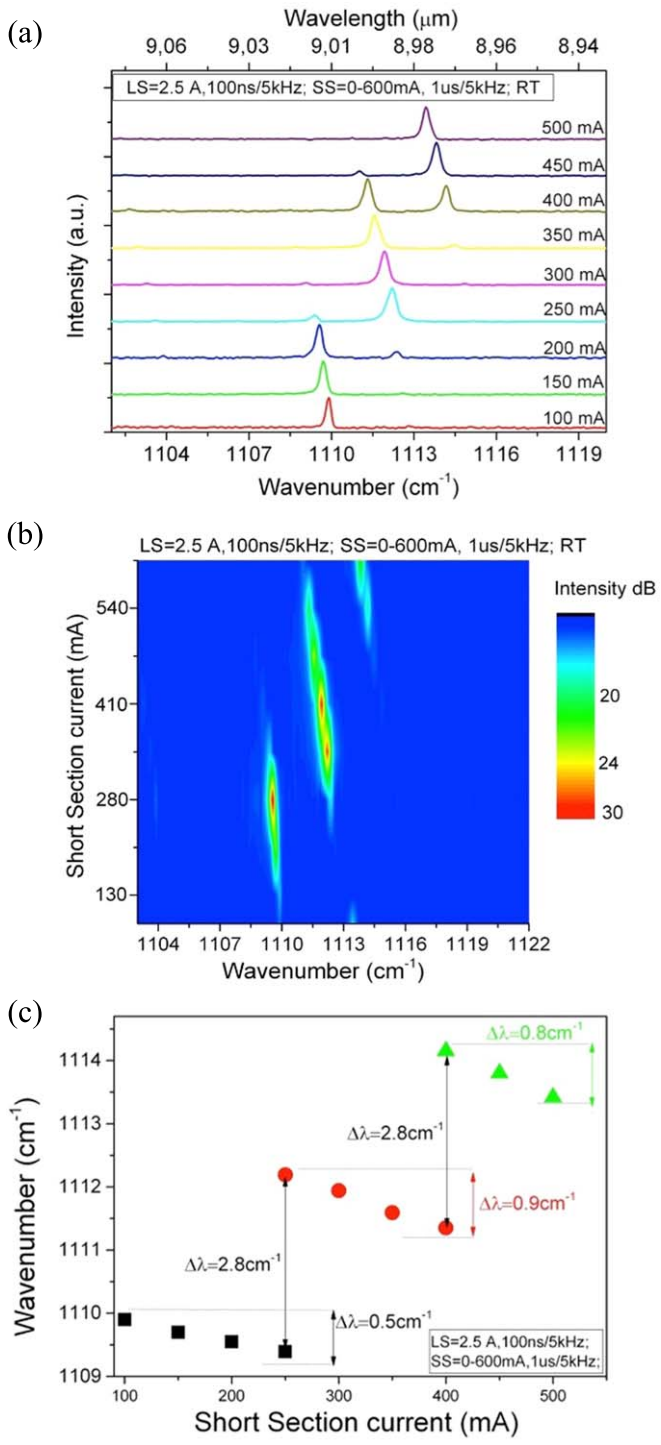

Figure 9. Vernier tuning at room temperature, with tuning power applied to the short section SS of the laser. (a) Spectral evolution, (b) spectral map of Vernier tuning, (c) tuning range versus short section current I_{SS}. The laser cavity length equals 2 mm and the mesa width equals 15 μm.

The discrete Vernier tuning has been also demonstrated. The laser with a 2 mm cavity length and a mesa width of 15 μm, cut in 1:3 proportions, was operated with the shorter section serving as the tuning section, and the longer section as the lasing section. The tuning section was heated by 1 μs long current pulses at a repetition rate of 5 kHz. The lasing section was driven by $I_{LS} = 2.5$ A, 100 ns pulses with 5 kHz repetition. The experimental data obtained for the investigated device are shown in figure 9.

The observed mode switching occurs when the effective reflectivity of the gap and the short cavity is aligned with a longitudinal mode of the active cavity. The tuning range was equal to 40 nm with a mode discrimination of ~30 dB.

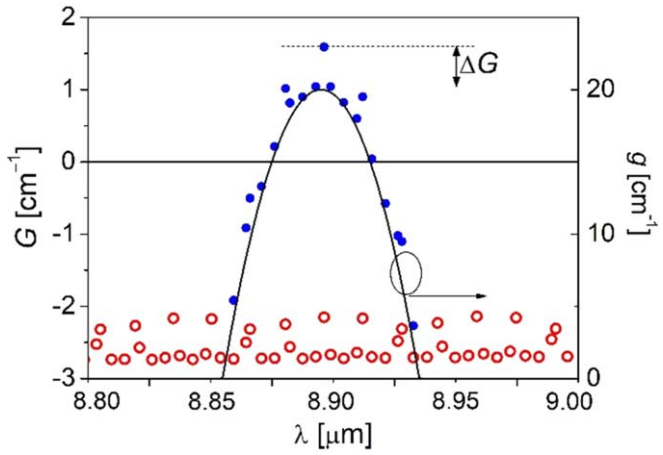

Figure 10. Modal gain (G) of the longitudinal modes as the function of the wavelength (λ) in the case of transparent active region ($g = 0$)—red circles; and the modal gain of the same modes in the case of assumed gain spectrum—blue dots. The black curve illustrates the material gain spectrum (g). ΔG is defined as the difference of the modal gain between the modes of the largest modal gain.

5. Numerical model and simulation results

Tuning of the single mode operation of CC QCLs should involve the optimization of the longitudinal design to discriminate the number of longitudinal modes, and select only one of them. The amount of lateral modes can be precisely controlled by the epitaxial design and by the parameters of the mesa etching [18], which assure a lateral fundamental mode operation. For the clarity of the considerations, the numerical analysis of any higher order lateral modes can be omitted. Therefore, a fully three-dimensional optical model can be replaced with a quasi three-dimensional effective index approach, which solves the Helmholtz equation separately for each direction [19]. This is computationally highly efficient and allows the effortless finding of lateral fundamental modes. The validation of such an approach confirmed acceptable accuracy in comparison to fully vectorial models in the case of the typical geometry of diode lasers [20]. Particularly, a one-dimensional transfer admittance method [21] is applied to solve the Helmholtz equation in each direction, since it reveals numerical stability in the analysis of the structures consisting of alternate thick and very thin layers [22].

The heating of the device is an important mechanism responsible for changing the refractive index of it and tuning the gain spectrum. The change of the refractive index of the cavity modifies the optical length and consequently changes the wavelength of the longitudinal modes. Since the typical longitudinally monolithic cavity of the edge-emitting laser is significantly larger than the emitted wavelength, the spectral distance between the longitudinal modes is very small. Such a modal structure does not put any constrains on the gain spectrum, which typically overlaps over a dozen of longitudinal modes. The emission wavelength hence is determined by the peak of the material gain spectrum.

In the case of the CC QCL considered here, the gain spectra of both cavities can be tuned separately by the injected pulse currents. Single mode operation can be achieved by overlapping both gain spectra and by fine overlapping of the most intense modes related to the mode combs of both cavities. Such thermal tuning of the device requires a very accurate three-dimensional thermal time dependent model [23] to take into account the evolution of the temperature distribution within the electrical pulse. The thermal and electrical models are described with great detail in [24].

The change of the temperature affects the band structure of the cascades and shifts the material gain peak. Figure 10 shows the modal gain of the longitudinal modes as the function of the wavelength in the considered structure, without and with the material gain. In the case of the monolithic cavity, the modal gain of all modes from the considered wavelength range is nearly the same in the slab without any gain spectrum. The division of the slab on two sections introduces the disturbance to the cavity. The modes that are simultaneously close to the resonance in both sections are favoured with respect to the modal gain. Imposition of the spectral gain is an additional factor favouring the modes. The modal gain increases in the case of the modes which wavelengths overlap the range of the positive material gain. Spectral shape of the gain favours the mode which wavelength is the closest to the gain peak. We introduce ΔG, which is the modal gain difference between two modes of the largest modal gains. We treat ΔG as the measure of the design ability to single mode operation.

Figure 11 illustrates the wavelengths of the modes for which the modal gain is larger than 0. Such modes will be called 'excited' modes. The current I_1 of the SS is varied in the range from 0 to 4 A while the current I_2 of the LS

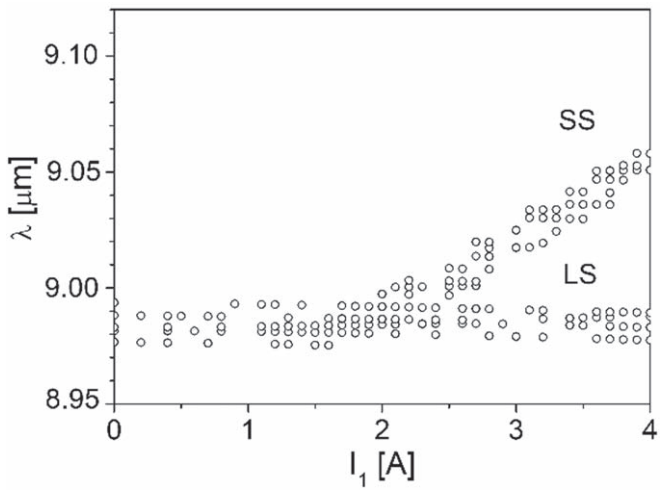

Figure 11. The wavelengths (λ) of the modes for which the modal gain is above zero as the function of the pulse current in the short section SS (I_1). The pulse current of long section LS (I_2) is kept constant and equals 0.9 A.

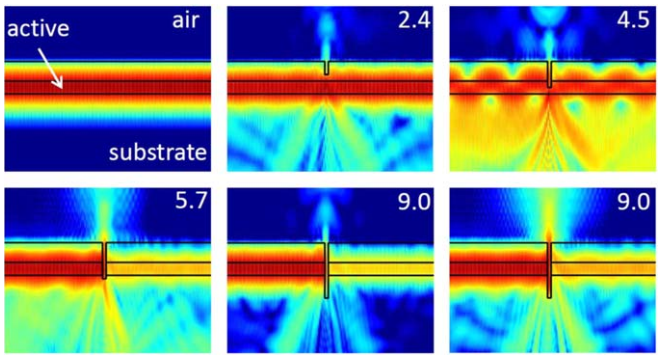

Figure 12. The distribution of CC modes for selected slot depths: 0, 2.4 μm, 4.5 μm, 5.7 μm and 9.0 μm.

is kept constant at 0.9 A. In the range of currents $0 < I_1 < 0.5$ A, the short section is biased below threshold and is absorbing, hence it acts as a filter of the modes of the higher modal gain. For I_1 above the ~0.5 A, a larger number of the modes appears in the laser spectrum, since the SS exceeds the threshold. A further increase of the current I_1 heats the short section and causes the gain shift. The shifting gain spectrum excites the modes of the longer wavelength. The configuration in which one of the sections is below the threshold, or where the gain spectra do not overlap, can support the single mode emission by selective absorption of the modes; however, such a mechanism is very inefficient. The most efficient configuration relates to the overlapping of the modes corresponding to the peaks of both gain spectra.

The influence of the slot depth on the modal structure of CC QCL has been studied with the use of a fully vectorial optical model (Plane Wave Admittance Method [21]). The simulation results are shown in figure 12. The slot width assumed for calculations was 9 μm. As the bottom of the slot coincides with the large mode intensity, it can be observed for etching depths of 4.5 and 5.7 μm that an increasing amount of energy is scattered towards the substrate, contributing to optical power dissipation. The slot of a significantly low refractive index introduced to the laser cavity becomes an obstacle for resonating light within the cavity. According to the Huygens–Fresnel principle, it behaves as a secondary source of electromagnetic wave and creates a new wavefront enabling propagation of the electromagnetic field in all directions. Hence the resonating light—which is diffracted at the edge of the slot—becomes redirected in all possible directions. Light diffracted toward substrate propagates under all possible angles; however light redirected toward the top surface is emitted in a relatively narrow angle, which is limited by the total internal reflection occurring at the top laser surface. The last two pictures present modes of the lowest modal loses in the structure with a 9.0 μm slot depth, which shows reduced scattering losses with respect to shallower etchings. This example illustrates that a deep etching reaching below the bottom waveguide layer reduces scattering and introduces an efficient air-gap between coupled cavities.

6. Conclusions

We have experimentally demonstrated the single mode operation of a CC AlInAs/InGaAs/InP quantum cascade laser. A side mode suppression ratio on the level of 43 dB was achieved by tuning the driving level of both sections of the laser. We have demonstrated a discrete Vernier tuning over the range of 40 nm. Using a three-dimensional, self-consistent model of physical phenomena in an edge emitting laser, we have investigated the influence of injected currents on the modal characteristics. The analysis confirmed in the experimental results that the most efficient single mode operation takes place in the case of relatively close current densities in both sections of CC QCLs, which assures the overlapping of the gain spectra of both sections. In such a configuration, the fine tuning of the currents allows one to favour the mode that coincides with the gain peaks, and suppress all others.

Acknowledgments

This work was supported by the Polish National Centre for Research and Development (NCBR) through projects PBS2/A3/15/2013 PROFIT and Techmatstrateg SENSE no. 2013/09/D/ST7/03966 and by National Science Centre (NCN) under project SONATA no. 2013/09/D/ST7/03966.

ORCID iDs

Maciej Bugajski https://orcid.org/0000-0001-8775-7521
Tomasz Czyszanowski https://orcid.org/0000-0002-0283-5074
Dorota Pierścińska https://orcid.org/0000-0001-5941-2147

References

[1] Faist J, Capasso F, Sivco D L, Sirtori C, Hutchinson A L and Cho A Y 1994 *Science* **264** 553
[2] Curl R F, Capasso F, Gmachl C, Kosterev A A, McManus B, Lewicki R, Pusharsky M, Wysocki G and Tittel F K 2010 *Chem. Phys. Lett.* **487** 1
[3] Zeller W, Naehle L, Fuchs P, Gerschuetz F, Hildebrandt L and Koeth J 2010 *Sensors* **10** 2492
[4] Coldren L A and Koch T L 1984 *IEEE J. Quantum Electron.* **20** 657
[5] Hvozdara L, Lugstein A, Gianordoli S, Schrenk W, Strasser G, Unterrainer K, Bertagnolli E and Gornik E 2000 *Appl. Phys. Lett.* **77** 1077
[6] Ross I M, Ng W H, Wilson L R, Luxmoore I J, Cockburn J W, Krysa A, Cullis A G and Roberts J S 2006 *Journal of Physics: Conference Series* **26** 215
[7] Fuchs P, Seufert J, Koeth J, Semmel J, Hofling S, Worschech L and Forchel A 2010 *Appl. Phys. Lett.* **97** 181111
[8] Meng B, Tao J, Li X H, Zeng Y Q, Wu S and Wang Q J 2014 *Appl. Phys. Lett.* **104** 201106
[9] Piersciński K, Pierścińska D, Pluska M, Gutowski P, Sankowska I, Karbownik P, Czerwinski A and Bugajski M 2015 *Journal of Applied Physics* **118** 133103
[10] Beck M, Hofstetter D, Aellen T, Faist J, Oesterle U, Ilegems M, Gini E and Melchior H 2002 *Science* **295** 301
[11] Gutowski P, Karbownik P, Trajnerowicz A, Pierściński K, Pierscińska D, Sankowska I, Kubacka-Traczyk J, Sakowicz M and Bugajski M 2014 *Photon. Lett. Poland* **6** 142
[12] Bugajski M *et al* 2014 *Phys. Status Solidi B* **251** 1144
[13] Hałdaś G, Kolek A and Tralle I 2011 *IEEE J. Quantum Electron.* **47** 878
[14] https://photond.com/products.htm
[15] Kolek A, Hałdaś G and Bugajski M 2012 *Appl. Phys. Lett.* **101** 061110
[16] Kolek A, Hałdaś G, Bugajski M, Pierściński K and Gutowski P 2015 *IEEE J. Selected Topics in Quantum Electronics* **21** 1200110
[17] Czerwinski A, Pluska M, Łaszcz A, Ratajczak J, Pierściński K, Pierścińska D, Gutowski P, Karbownik P and Bugajski M 2015 *Microelectronics Reliability* **55** 2142
[18] Yu N, Diehl L, Cubukcu E, Pflügl C, Bour D, Corzine S, Zhu J, Höfler G, Crozier K B and Capasso F 2007 *Opt. Express* **15** 13227
[19] Buus J 1982 *IEEE J. Quant. Electron.* **18** 1883
[20] Czyszanowski T and Nakwaski W 2007 *Opto-Electron. Rev.* **15** 88
[21] Dems M, Kotynski R and Panajotov K 2005 *Opt. Express* **13** 3196
[22] Helfert S F and Pregla R 1998 *J. Lightwave Technol.* **16** 1694
[23] Sarzała R P, Wasiak M and Nakwaski W 2011 *Photon. Lett. Poland* **3** 52
[24] Kuc M, Sarzała R P, Czyszanowski T and Bugajski M 2016 *Proc. of SPIE* **9767** 97671V-1